On the Robustness and Accuracy of Large-Eddy Simulation in Predicting Complex Internal Flow of a Gas-Turbine Combustor

Zheng Qiao (乔正),[1,2] Yu Chen (陈与),[1,2] Kaidi Wan (万凯迪),[3,4] and Yu Lv* (吕钰)[1,2]

[1)] *State Key Laboratory of Nonlinear Mechanics, Institute of Mechanics, Chinese Academy of Sciences, Beijing, 100190, China*

[2)] *School of Engineering Sciences, University of Chinese Academy of Sciences, Beijing, 101408, China*

[3)] *Aircraft and Propulsion Laboratory, Ningbo Institute of Technology, Beihang University, Ningbo 315832, China*

[4)] *National Laboratory for Computational Fluid Dynamics, School of Aeronautic Science and Engineering, Beihang University, Beijing 100191, China*

(*Electronic mail: lvyu@imech.ac.cn)

The objective of this study is to evaluate the effects of numerical and model setups on the large-eddy simulation (LES) predictive capability for the internal flow of a propulsion-relevant configuration. The specific focus is placed on assessing the LES technique with lower mesh resolutions, which is of technological relevance to practical industrial design. A set of Riemann flux formulations and commonly used subgrid-scale models are considered in this work to produce a hierarchy of LES setups with different dissipation effects (both numerically and physically). The LES results obtained from different setups are compared qualitatively in terms of the key flow characteristics, and evaluated quantitatively against the experimental measurements. The error landscape is generated to reveal the predictive qualities of different LES setups. The study shows that the choice of numerical flux formulation plays a prominent role in governing the general flow patterns, while the effect of subgrid-scale model is mainly manifested in transient flow characteristics, such as vortex breakdown and swirl-induced vortical structures. Based on the error analysis, it is found that lower dissipative LES setup is not always beneficial to the LES accuracy. This is in contrast to the commonly accepted understanding in literature for LES, which was established solely with canonical flow configurations.

I. INTRODUCTION

Analysis and design of aero-propulsion systems often require high-fidelity computational fluid-dynamic techniques to resolve unsteady flow features and capture flame dynamics. In particular, the large-eddy simulation (LES) method has gained the remarkable success over the past decade in the computational analysis of various combustion devices with industrial-level complexity[1,2]. The prevalent use of LES in design has greatly benefited the resolution of a number of combustion technological problems, such as the reduction of noise/pollutant emissions[3–6], the characterization of ignition[7,8] and blow-off limits[9–11], and the identification of thermoacoustic behaviors[12–14]. In spite of those achievements, it should be clarified that LES remains rather time-consuming for the purpose of industrial design and requires considerable computational cost when applied to investigate the complex flow configurations of practical relevance. In order to meet the timeliness requirement, the design-oriented computational analysis is often carried out on relatively coarser grids to reduce the computational cost. Simulations as such might not be as rigorous as those for academic studies (which require at least 80 % turbulent kinetic energy to be resolved[15]) but have great significance in a practical sense.

The internal flows particularly in industry-type combustion devices feature a number of complex flow effects, such as shear layer, wall boundary layer, flow separation and swirling flow. These effects are commonly associated with large-scale coherent structures, of which the time-accurate description, based on the LES technique, becomes necessary. However, for LES to capture such complex turbulent flows on relatively coarse grids, its reliability becomes a remarkable concern. With lower numerical resolutions LES results often exhibit strong sensitivities to the choice of numerical schemes[16,17] and subgrid-scale models[18]. The effort of pursuing high-order accuracy and non-dissipative schemes might not be preferable, when it comes to LES of complex flows in realistic geometries[19]. To ensure the robust solution procedure, it is almost unavoidable to introduce certain amounts of numerical dissipation to tackle the numerical instabilities which may be associated with distorted or highly stretched grids, local geometrical singularity or under-resolved flow scales. As such, the LES accuracy has to be compromised to some extent. The dissipative errors introduced by numerics may have multi-faceted influences on LES predictions. For instance, it can impact the mixing characteristics in turbulent shear layers[17,20], alter the dynamics and evolution of large-scale vortical structures, and weaken the flow separation. The assessment studies[21,22] considering the Taylor-Green Vortex test case showed that even with the same mesh different numerical schemes might lead to very different predictions of enstrophy. To obtain better solutions, it generally requires the scheme to have well-controlled dissipative and dispersive properties. A concerted workshop effort[23] also revealed the influence of numerical dissipation in LES of separated flows. It is found that results based on dissipative schemes tend to predict short recirculation zones behind a bluff body.

Besides the numerics, the influence of subgrid-scale (SGS) model in LES should not be understated as well. It was found that the dynamic models, which typically have superior performance over the standard Smagorinsky model in channel or shear flows, provide much poorer predictions of flow separation due to the underestimation of near-wall stress[24]. Similar deficiency associated with the dynamic model was also alluded in the workshop results[23]. Robustness issues of SGS model were recognized in modeling turbulent flows dominated with coherent or swirling vortex. With the consideration of the Taylor-Green Vortex case, Dairay et al.[25] conducted an interesting assessment on LES and showed that Smagorinsky models of different versions result in poor statistical convergences of characteristic quantities; moreover, applying subgrid-scale model does not effectively mask the numerical errors. The analysis by da Silva and Pereira[26] showed that several commonly used SGS models cause excessive vorticity dissipation. In order to better preserve the large-scale coherent structures, vorticity preserving LES methodologies were developed to avoid introducing excessive dissipation to the regions dominated by large-scale vortical motions. Recent efforts are recognized in this regard. For example, Chapeliar et al.[27] developed an eddy-viscosity correction approach, in which the SGS terms are adaptively applied according to the local entropy value. Foti and Duraisamy[28] proposed a vorticity-based formulation, in which the physically-consistent SGS behavior is mimicked numerically by a truncation term. Coherent-structure or vortex based SGS models[29–34] were also developed previously in order to improve LES model accuracy and address the robustness issues.

Given the aforementioned challenges to make use of the LES technique at lower resolution settings, it is thereby important to understand the behaviors of numerical and model errors and evaluate the results obtained from different LES setups. The objective of this study is to carry out error landscape analysis on coarse-grid LES, and analyze the impact of errors resulting from different numerical schemes and subgrid-scale models on LES predictions.

The main difference of our study from the previous assessments[21,26,35] is that we consider the internal flows in a realistic combustor geometry rather than classical test cases in simple configurations. Therefore, the findings are expected to be more instructive to practical LES for industrial design. In particular, our analysis focus on the following questions related to coarse-grid LES:

- how do the numerical and modeled dissipation effects influence the key flow characteristics?
- how do the numerical and model errors interplay with each other?
- of the errors from the SGS model and numerical scheme, which one is more relevant to the robustness?

To better address the above questions, the remainder of this work is structured as follows. The mathematical formulation and numerical method are outlined firstly in Sec. II, followed by the flow configuration and computational setup introduced in Sec. III. The comprehensive evaluations of LES results, along with the error analysis, are carried out in Sec. IV. Therein, the influence of LES setups on the predictive quality is investigated in detail. The paper finishes with conclusions in Sec. V.

II. MATHEMATICAL MODEL AND NUMERICAL METHOD

A. Governing Equations

In the context of large-eddy simulation, the notation of grid-dependent filter is introduced to separate the resolved and subfilter scales of turbulent flows. The LES-filtered quantity may be expressed as:

$$\overline{\phi} = \int_{-\infty}^{\infty} \mathcal{G}(x - x')\phi(x')dx' \ , \tag{1}$$

where $\mathcal{G}$ represents a filter kernel dependent on the grid size. As a result, the LES-filtered Navier-Stokes equations can be written as:

$$\begin{aligned}
\partial_t\overline{\rho} + \nabla\cdot(\overline{\rho}\widetilde{\boldsymbol{u}}) &= 0, & \text{(2a)}\\
\partial_t(\overline{\rho}\widetilde{\boldsymbol{u}}) + \nabla\cdot(\overline{\rho}\widetilde{\boldsymbol{u}}\widetilde{\boldsymbol{u}}^T) + \nabla\overline{p} &= \nabla\cdot\left(\overline{\boldsymbol{\tau}} - \boldsymbol{\tau}^{SGS}\right), & \text{(2b)}\\
\partial_t(\overline{\rho}\widetilde{E}) + \nabla\cdot(\widetilde{\boldsymbol{u}}(\overline{\rho}\widetilde{E} + \overline{p})) &= -\nabla\cdot\left(\overline{\boldsymbol{q}} + \boldsymbol{q}^{SGS}\right) + \nabla\cdot((\overline{\boldsymbol{\tau}} + \boldsymbol{\tau}^{SGS})\cdot\widetilde{\boldsymbol{u}}). & \text{(2c)}
\end{aligned}$$

where ρ is density, u is velocity, p is pressure and E is total energy. The Reynolds- and Favre-filtered quantities are denoted as $\bar{(\cdot)}$ and $\widetilde{(\cdot)}$, respectively. The filtered viscous stress tensor and heat flux take the forms of

$$\overline{\boldsymbol{\tau}} = \mu\left(\nabla\widetilde{\boldsymbol{u}} + (\nabla\widetilde{\boldsymbol{u}})^T\right) - \frac{2}{3}\mu(\nabla\cdot\widetilde{\boldsymbol{u}})\mathbf{I}, \tag{3a}$$

$$\overline{\boldsymbol{q}} = -\kappa\nabla\widetilde{T}, \tag{3b}$$

where μ and κ are the molecular viscosity and thermal conductivity. The terms, denoted by the superscript "SGS", represent the subgrid-scale quantities. The subgrid-scale stress and energy flux can be treated via the eddy-viscosity closure model,

$$-\boldsymbol{\tau}^{SGS} = -(\bar{\rho}\widetilde{\boldsymbol{u}\boldsymbol{u}^T} - \bar{\rho}\widetilde{\boldsymbol{u}}\widetilde{\boldsymbol{u}}^T) \approx \mu_t\left(\nabla\widetilde{\boldsymbol{u}} + (\nabla\widetilde{\boldsymbol{u}})^T\right) - \frac{2}{3}\mu_t(\nabla\cdot\widetilde{\boldsymbol{u}})\mathbf{I}\ , \tag{4a}$$

$$-\boldsymbol{q}^{SGS} = -(\bar{\rho}\widetilde{\boldsymbol{u}H} - \bar{\rho}\widetilde{\boldsymbol{u}}\widetilde{H}) \approx \frac{\mu_t c_p}{\mathrm{Pr}_t}\nabla\widetilde{T}\ , \tag{4b}$$

in which T is temperature, c_p is the heat capacity, μ_t is the eddy viscosity, and Pr_t is the turbulent Prandtl number. The system of Eq. (2) is closed with the equation of state,

$$\widetilde{p} \approx (\gamma - 1)(\bar{\rho}\widetilde{E} - \frac{1}{2}\bar{\rho}|\widetilde{\boldsymbol{u}}|^2)\ , \tag{5}$$

in which γ is the adiabatic index and taken as 1.4 for air.

B. Discretization Scheme

In this work, the governing equations are discretized using a classical reconstruction-based finite-volume method[36]. The key idea is illustrated schematically in Figure 1. In each cell, we aim to reconstruct a solution polynomial of $\mathcal{P}$ using the piecewise solutions in the local cell and direct neighbors. For hexahedral cells which have six neighbors, a quadratic polynomial with a set of basis functions $\{1,\ x,\ y,\ z,\ x^2,\ y^2,\ z^2\}$ can be reconstructed; and for tetrahedral cells which have four neighbors, a linear polynomial $\mathcal{P}^1$ with the basis functions $\{1,\ x,\ y,\ z\}$ is reconstructed through a least-square procedure. On each edge, the reconstructed polynomials of the left and right cells are interpolated onto the edge centroid to formulate the interfacial numerical flux. The reconstruction is performed based on the primitive variables, which is found to be more reliable[35]. It is also noteworthy that for a scalar conservation law, this scheme reverts to a fourth-order central differencing on Cartesian meshes.

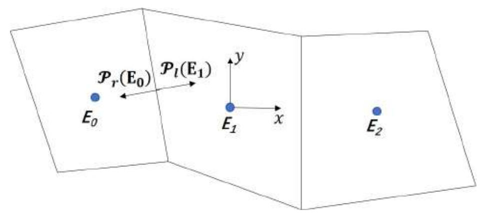

FIG. 1. Demonstration of numerical discretization method (E_0, E_1 and E_2 represent three adjacent cells; $\mathcal{P}$ denotes the reconstructed polynomial in each cell; "l" and "r" indicate the left and right edges of the corresponding cell).

With the implemented finite-volume scheme, the spatially discretized governing equations may be written as a set of cell-local ordinary differential equations with respect to time,

$$\frac{d\mathbf{U}}{dt} = \mathbf{R} \; , \tag{6}$$

in which $\mathbf{R}$ is the residual assembled in each cell and $\mathbf{U}$ represents the solution vector. $\mathbf{U}$ is then updated in time with a strong-stability preserving 3rd-order Runge-Kutta scheme:

$$\mathbf{U}^{(1)} = \mathbf{U}^n + \Delta t \mathbf{R}\left(\mathbf{U}^n\right) \; , \tag{7a}$$

$$\mathbf{U}^{(2)} = \frac{3}{4}\mathbf{U}^n + \frac{1}{4}\left(\mathbf{U}^{(1)} + \Delta t \mathbf{R}(\mathbf{U}^{(1)})\right) \; , \tag{7b}$$

$$\mathbf{U}^{n+1} = \frac{1}{3}\mathbf{U}^n + \frac{2}{3}\left(\mathbf{U}^{(2)} + \Delta t \mathbf{R}(\mathbf{U}^{(2)})\right) \; . \tag{7c}$$

The above numerical method has been implemented in our SUPES (Scalable mUlti-Physics Entropy-Stable) solver, which is an in-house code developed for several years[37–39]. The solver is equipped with a number of flux formulations and subgrid-scale models, and has been validated in a number of canonical flow test cases. Moreover, the wall-modeling capability has been developed to account for the wall effects in LES. The wall modeling capability is based on the equilibrium wall model[40] and the LES information of the first two off-wall cells[41] are utilized to construct the wall shear stress. Moreover, an algebraic-based treatment[38] was developed recently to simplify the implementation and reduce computational costs. In the present study, the SUPES solver is used to assess the performance of coarse-grid LES with the various numerical and model setups.

III. FLOW CONFIGURATION AND COMPUTATIONAL SETUP

A. Combustor Geometry and Mesh

In this work, we consider the gas-turbine model combustor (GTMC), experimentally investigated by Meier et al.[42,43], as the target geometry. Figure 2 provides the schematic of the combustor, which consists of a plenum, a swirler, an injector, a chamber and an exhaust chimney. The air stream (Stream 1) from the plenum divides into two branches, which, respectively, pass through the upper and lower sets of vanes inside the swirler. The two branches of air enter the combustor chamber through the injector nozzles, along with the fuel supply stream (Stream 2). The fuel is substituted by air in the cold-flow operating condition. The injector section consists of a central air nozzle, an annular fuel nozzle, and a co-annular air nozzle. The central nozzle has a diameter of 15 mm and the co-annular air nozzle has an inner diameter of 17 mm and a outer diameter of 25 mm. The chamber is in a rectangular shape with a dimension of 110 mm in height and 85 mm in width. The exhaust chimney is a tube with a diameter of 40 mm. The mass flow rates of Streams 1 and 2 are 19.74 g/s and 1.256 g/s[44], respectively, calculated in terms of air at the room temperature and ambient pressure. Because of the non-trivial combustor geometry, both the values of Reynolds number and Mach number vary by location. The Reynolds numbers, at the plenum inlet, burner inner nozzle, burner annulus and combustor outlet, are estimated to be 108,000, 63,500, 65,000 and 50,000, respectively. The Mach numbers corresponding to the above locations in order are 0.26, 0.18, 0.1 and 0.05, respectively. The swirler has a complex geometry and its details may be observed in the generated mesh shown in Figure 3. The reason why we consider this flow configuration is that: *i*) it is of practical relevance to propulsion applications; and *ii*) previous LES studies on this specific geometry exhibit inconsistent solutions and considerable prediction errors (in particular for the cold-flow case)[45]. Therefore, this flow configuration is an ideal one to challenge the robustness of LES technique, so that we can identify the influencing factors, especially numerical scheme and SGS model, to the predictive quality of LES.

Figure 3 illustrates the computational mesh employed in this study, which is divided into the chamber part (a) and the lower part (b) including the swirler and the plenum for clarity. The whole computational domain consists of 8 million hexahedral cells in total, which breaks

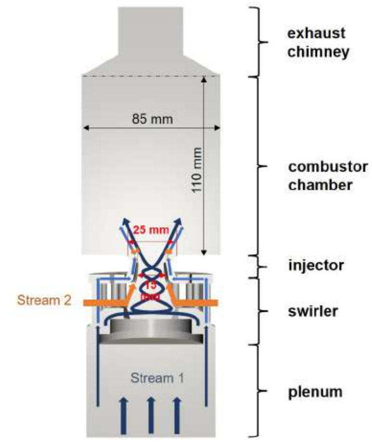

FIG. 2. Schematic of the GTMC combustor[42,43]

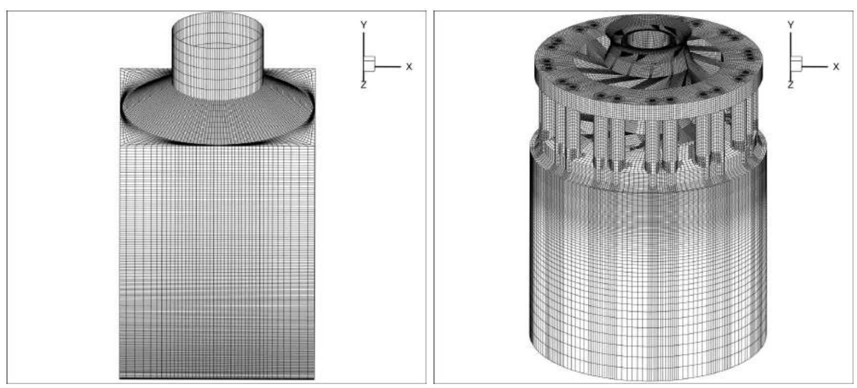

(a) (b)

FIG. 3. Schematic of the computational mesh for parts of (a) combustor chamber and exhaust chimney and (b) plenum, swirler and injector.

down to 0.65 million for the plenum, 3.1 million for the swirler, 4.1 million for the joint of the injector and chamber, and 0.15 million for the rest. Substantial effort and time have been devoted to meshing the swirler. The meshing process begins with cutting the swirler into smaller components, such as the cylindrical and rectangular flow passages. These components can be easily meshed with hexahedral cells. Once the swirler mesh is completed, the parts of the plenum and chamber are then meshed by extruding downward and upward, respectively. Previous studies[46–48] showed that the outflow boundary condition may have considerable influence on the internal flow behaviors. To avoid the boundary effects, our actual outflow boundary is extended to the far field, and a characteristic boundary condition is imposed there. The mesh resolution is purposely chosen so that the LES calculations are performed with affordable cost and importantly the numerical and model errors can be revealed in the LES results. Compared to the mesh used previously in the hybrid turbulence model study[44], the mesh resolution considered here is proven sufficient to produce accurate predictions of mean-flow statistics. On the other hand, based on the findings from previous LES investigations[45,49], the employed mesh is still relatively coarser so that LES predictions show appreciable sensitivities to the numerical and model setups. As emphasized in the introduction, this work focuses on assessing coarse-grid LES for industrial-type flow configurations; therefore, the flow configuration and computational mesh are purposely selected for this objective.

B. Computational Setup

Six computational setups are considered in this study to evaluate the effects of flux formulation and subgrid-scale model on the simulation results. Three different types of Riemann solvers are selected for test, including the HLLC[50], AUSM+[51] and kinetic-energy-preserving (KEP)[52] flux formulations. These solvers are commonly used in scale-resolving simulations and presumably introduce the amounts of numerical diffusion in a descending order. The AUSM+ scheme[51] was developed to avoid excessive dissipation at low-Mach flow conditions; meanwhile, the KEP scheme[52] is a non-dissipative scheme that preserves the integral of kinetic energy (on structured periodic meshes[52]). As for the SGS model, both the standard Smagorinsky model[53] and the Vreman model[54] are considered, because both models are extensively used in combustion modeling and behave differently in terms of subgrid-scale dissipation[55]. The Vreman model is found to be as accurate as the dynamic Smagorinsky model[56]. With the above schemes and models, a set of LES experiments are designed. Each case with its own specific setup is given in Table I. The CFL number in our LES is set to 0.7 and the corresponding time step is about 10^{-8} s.

TABLE I. LES setup for each case

Case No.	Riemann solver	SGS model
1	HLLC	Smag.
2	HLLC	Vreman
3	AUSM+	Smag.
4	AUSM+	Vreman
5	KEP	Smag.
6	KEP	Vreman

IV. RESULTS AND DISCUSSIONS

In this part, the LES results of different computational setups are presented, along which the influences of numerical and model errors on the predicted flow characteristics are discussed.

A. Instantaneous flow structures

In this part, our focus is placed on the instantaneous flow structures predicted in the LES results. Figure 4 provides a global view of the flow field inside the combustor. As shown, a fast inflow jet penetrates the plenum and impinges onto the surface wall before slowing down. The air stream then passes through the swirler to generate spin motion. A helical structure is featured near the injector region and the stable recirculation zone is created by the swirl. Inside the chamber, the axial velocity exhibits a V-shape profile, which will be analyzed in detail later. Close to the exhaust chimney, a tornado-like flow pattern is present because of the radial geometrical contraction. Figure 5 shows the instantaneous axial velocity profiles and the streamlines in the six LES cases. The internal recirculation zone (IRZ) induced by the swirl is a clear feature of the flow field. Moreover, it is notable that the fluctuating flow field is dominated by vortex breakdown due to the strong shear effect. Given the specific flow configuration, a shear layer arises from the large velocity gradient between the swirl jet and central backflow of IRZ. Along this inner shear layer, a set of large-scale vortical structures are present in an alternating pattern and constantly oscillating. Such a flow pattern is related to the so-call precessing vortex core (PVC). PVC is a helical coherent

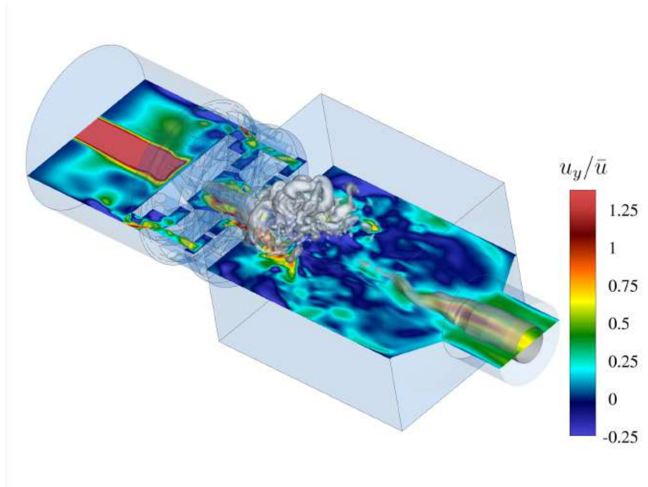

FIG. 4. Instantaneous flow field inside the combustor geometry (vortical structure visualized by pressure iso-surfaces and cut-plane colored by the axial velocity, normalized by the mean axial velocity at the nozzle outlet, is around 40 m/s).

structure that wraps around the IRZ and precesses along the central axis. PVC is commonly found in the swirling flow configurations[57–60] and also recognized in our LES results. The PVC structures are visualized using pressure iso-surface and exhibited in the set of plots in Table II. As shown, the spiral structure of PVC winds along the central axial and breaks down to small pieces downstream. The alternating vortices mentioned above in Figure 5 actually result from the intersection between the PVC spirals and the cut-plane of $z = 0$. These intersecting vortices are convected downstream until the breakdown takes place. The vortex breakdown leads to smaller scales, represented by localized high-speed spots scattered downstream. It is also noted that there is another shear layer situated between the jetting and the outer recirculation zone (ORZ), which we call the outer shear layer. The outer shear layer also induces shed vortices; however, the breakdown is weaker because of the smaller velocity gradient. Overall, the jetting inflow demonstrates a wake-like behavior.

We now proceed to examine the impact of numerical and model settings on transient flow characteristics. Reduction in numerical dissipation results in a more oscillatory flow field, along with a faster decay of axial velocity and a quicker expansion of the swirl jet

	$p/p_{\mathrm{ref}} = 0.984$	$p/p_{\mathrm{ref}} = 0.989$	$p/p_{\mathrm{ref}} = 0.994$
Case 1 HLLC & Smag.	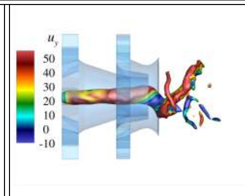	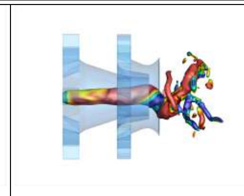	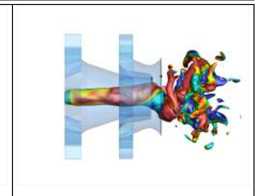
Case 2 HLLC & Vreman	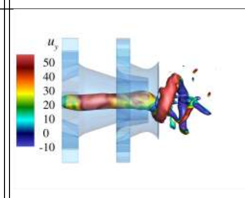	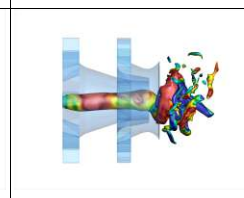	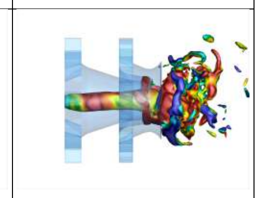
Case 3 AUSM+ & Smag.	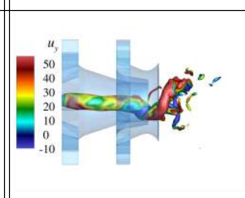	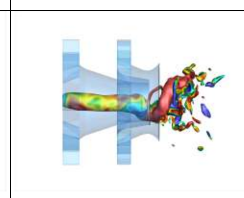	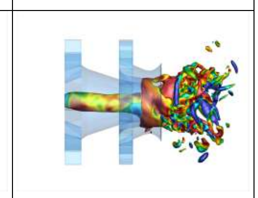
Case 4 AUSM+ & Vreman	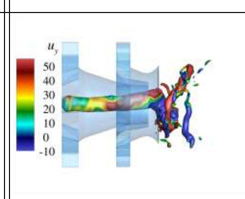	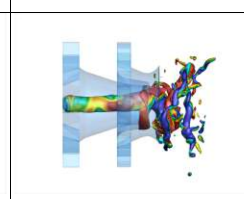	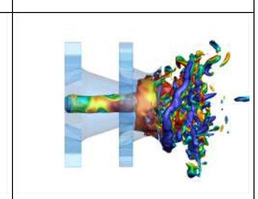
Case 5 KEP & Smag.	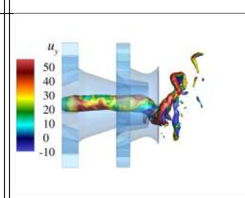	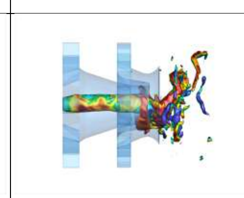	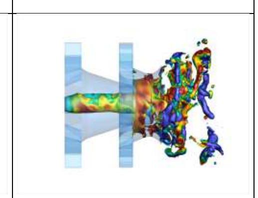
Case 6 KEP & Vreman	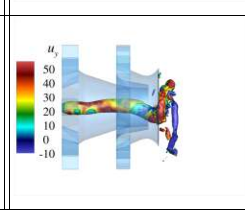	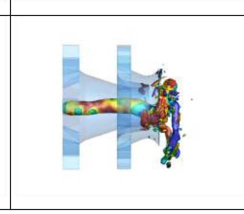	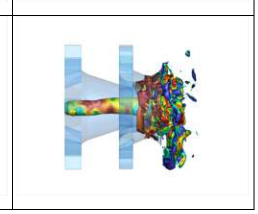

TABLE II. Precessing vortex cores (PVC) are visualized by various nondimensional pressure iso-surfaces, which are normalized by $p_{\mathrm{ref}} = 101325$ Pa and colored by the axial velocity in each case.

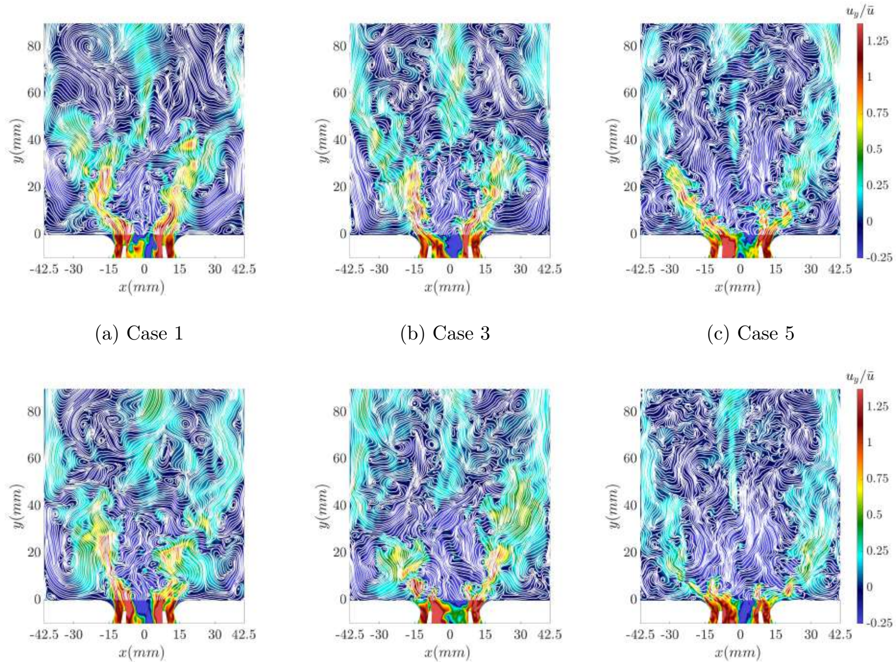

(a) Case 1 (b) Case 3 (c) Case 5

(d) Case 2 (e) Case 4 (f) Case 6

FIG. 5. Instantaneous flow fields of six different cases: (a) HLLC & Smag., (b) AUSM+ & Smag., (c) KEP & Smag., (d) HLLC & Vreman, (e) AUSM+ & Vreman, and (f) KEP & Vreman. Color contours–streamwise velocity, normalized by the mean axial velocity at the nozzle outlet, is around 40 m/s; and white lines–streamlines.

along the radial direction. When the flux formulation is changed to the KEP scheme, the velocity profile is significantly flattened. For instance, Case 6 even witnesses the formation of Coanda jet[61]. Coanda jet, although may possibly appear as a hydrodynamic feature, seems a non-physical artifact here, which is inconsistent with the previous findings[42,44]. The changes in PVC topology also reflect the influence of numerical schemes. When the flux formulation switches to ASUM+ from HLLC, the LES results show thinner, more elongated spirals and smaller fragments, as seen in Figure II. With the KEP scheme, further reduction in dissipation causes earlier vortex breakdown and meanwhile the PVC is dispersed out more quickly, which coincides with the excessive IRZ expansion observed in Figure 5. The effect

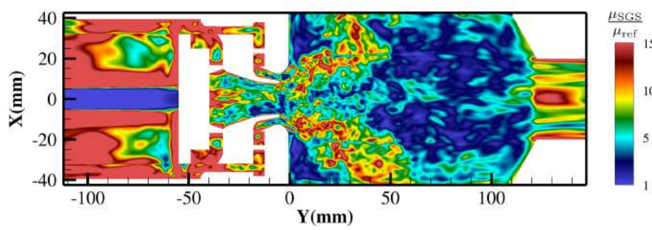

(a) Case 3: AUSM+ & Smag.

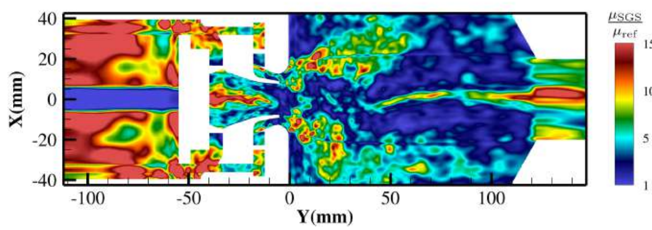

(b) Case 4: AUSM+ & Vreman

FIG. 6. Instantaneous nondimensional eddy viscosity field of two cases: (a) AUSM+ & Smag., and (b) AUSM+ & Vreman, which are normalized by $\mu_{\mathrm{ref}} = 1.8e^{-5}$ Pa·s.

of SGS model becomes more revealing in the instantaneous flow field as compared to that in the mean flow. In Figure 5, we in pair compare the results obtained with Vreman SGS model (Cases 2, 4 and 6), to those obtained with the classical Smagorinsky model (Cases 1, 3 and 5). It is observed in Cases 2, 4, and 6 that the vortex breakdown takes place earlier (also evidenced in the PVC structures in Table II); as a result, the potential core of the jet becomes shorter and the decay of axial momentum is more evident. Those behaviors are likely attributed to the lower magnitude of eddy viscosity given by the Vreman model. Figure 6 provides the distributions of eddy viscosity in Cases 3 and 4. In comparison, the eddy viscosity from the Vreman model is much more localized around the swirling jet and has a smaller value than the Smagorinsky model. Similar findings were reported in the literature. Pinho & Muniz[62] performed a set of LES cases of turbulent jet flows with the classical Smagorinsky SGS model to investigate the effects of the model coefficient on the LES solutions. It was found that the decrease of the model coefficient (equivalently, reducing the eddy viscosity) results in an earlier jet breakdown and a shorter potential core. Their study has well corroborated our finding here.

B. Mean flow-field characteristics

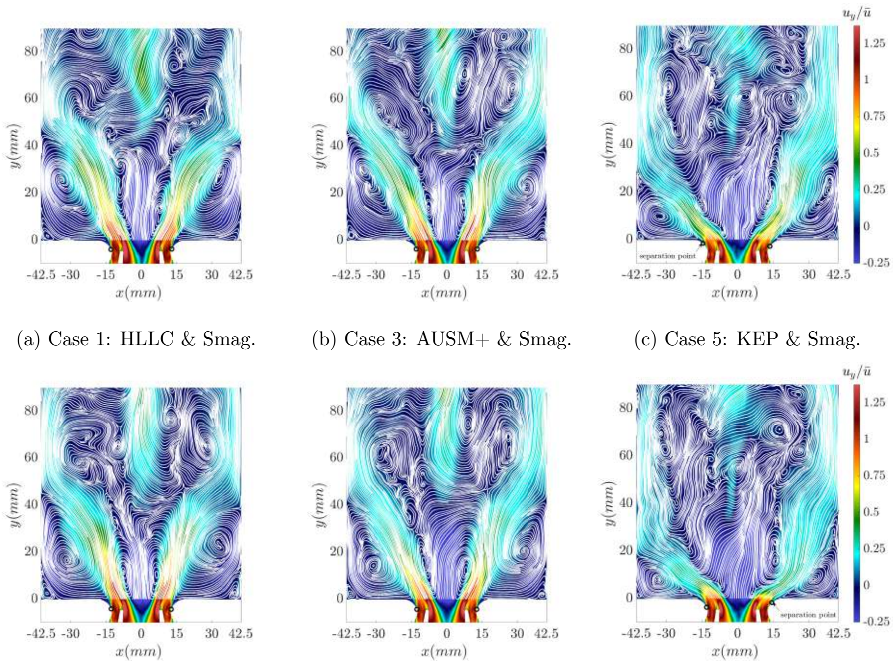

(a) Case 1: HLLC & Smag. (b) Case 3: AUSM+ & Smag. (c) Case 5: KEP & Smag.

(d) Case 2: HLLC & Vreman (e) Case 4: AUSM+ & Vreman (f) Case 6: KEP & Vreman

FIG. 7. Non-dimensional time-averaged streamwise velocity fields and streamline plots in the LES predictions with different solver settings: (a) HLLC & Smag., (b) AUSM+ & Smag., (c) KEP & Smag., (d) HLLC & Vreman, (e) AUSM+ & Vreman, and (f) KEP & Vreman. The time-averaged streamwise velocity fields are normalized by the mean axial velocity ($\bar{u}$ = 40 m/s) at the nozzle outlet. Separation points are marked by ∘.

Figure 7 shows the time-averaged streamwise velocity profiles, along with the streamlines on the $z = 0$ plane. The flow pattern generally assembles that illustrated in Figure 5 for each case. As shown in the velocity fields, two inflow streams after passing the swirler quickly merge into a single stream at the nozzle exit, and inside the chamber the V-shape velocity profile is clearly visualized. From the streamline patterns, it is observed that the

IRZ is generated along the center axis due to the swirl-induced lower pressure; on the other hand, the ORZ are present as the air from the corner is entrained into the inflow jet. These flow features agree well with the findings from the experimental measurements[42] and the previous numerical investigations[44,45]. At the chamber exit fluid flow exhibit acceleration due to converging geometry and an elongated fast-stream region become notable. In this region, the fluid flow exhibit tornado-like rotating pattern along the azimuthal direction[63,64].

The LES predictions in different cases are compared. The numerical flux shows considerable influence on the flow field. In particular, when KEP flux formulation is utilized, the velocity profile and streamline become rather different from those of the other cases. The diverging angle of the V-shape velocity profile is drastically enlarged. As a result, the IRZ, in this case, is expanded and the size of ORZ becomes much smaller. It is also noted that the separation no longer happens inside the nozzle part and the separation point of the inflow stream moves further downstream into the chamber. In contrast to the KEP scheme, the separation points in the other cases with HLLC and AUSM+ schemes are located on the wall of the exit diffuser of the nozzle, which is in fact a consistent feature with the previous simulation results[44]. The impact on the velocity prediction will be quantified later in Sec. IV C, but here the qualitative changes due to the choice of numerical flux have already become evident. Apart from the numerical factor, the SGS model seems to have limited effects on the time-averaged flow field, even though the profiles of eddy viscosity resulting from the different SGS models considered are quite different (see Figure 6).

C. Comparison to experimental data

To perform a quantitative assessment on the accuracy of LES predictions, we compare the predicted statistical quantities with the experimental data. Figure 8 shows the profiles of time-averaged axial (u_y), radial (u_x) and tangential (u_z) velocity components with the LDA measurements[44] at several axial positions. The axial velocity shows a two-peak structure; the two peaks are gradually smoothened out as the momentum mixing proceeds. The IRZ corresponds to the negative axial velocity at the center. Meanwhile, the ORZ may be recognized from the radial velocity profile, where the inward motion of the fluid is evident in the outer range of the x-axis. As for the tangential velocity profile, it is interesting to see that two spikes are present near the injector exit and situated at the inner and outer shear layers, respectively[45]. The two spikes merge into a single peak downstream. Near the exhaust chimney, the rotation remains persistent as seen from the tangential velocity because of the tornado-like vortical structure[44,64]. Meanwhile, a central peak is exhibited in the axial velocity due to the geometrical contraction. We now examine the LES predictions with different numerical and model settings. In Cases 1-4 where HLLC or AUSM+ flux is employed, the predicted initial peak locations of axial velocity slightly deviate from the experimental data. In addition, the peak magnitudes of radial and tangential velocity components are over-predicted in Cases 1-4. Except for these errors, the velocity predictions are in good agreement with the experimental data. This fact that variants of LES setups lead to similar results confirms the robustness of LES for applications to complex internal flows. However, when KEP flux scheme is used in Cases 5 and 6, considerable errors are present in the velocity predictions, and the flow field experiences excessive radial expansion as shown in Figure 7. The finding that LES accuracy worsens with reduced numerical dissipation contradicts the common notion that a lower dissipation scheme is preferred for LES. This is attributed to the flow configuration considered in this work, which apparently poses nuanced requirements on the flux formulation. Previous numerical assessments only considered simple flow configurations, such as homogeneous turbulence or channel flow, which does not involve the strong swirling and the sophisticated vortex breakdown as discussed previously in Sec. IV B and IV A. The effect of SGS model seems only manifested in the predictions of radial velocity. The Vreman model tends to cause faster decay of radial velocity (e.g., at $h = 20$ and 90 mm), resulting in relatively larger errors. Note that at the sidewall location $x = -40$ mm a few experiment data of u_x are exceptionally large. Up to now none of the existing LES/DES cases[44,45,49,65] is able to mitigate the discrepancy at this specific location. In general, the velocity profile should conform to the no-slip condition at the wall. Unreasonably large velocity should not be present there. This specific discrepancy is likely related to the experiment factors, which may result from the lack of sampling particles for velocity measurement near the wall.

Figure 9 shows the root-mean-square (RMS) values of axial, radial and tangential velocity components predicted in different LES cases. It is evident that near the injector exit, the velocity fluctuation levels exhibit two types of peaks which correspond to the inner and outer shear layers, respectively. Along the inner layer (associated with the IRZ), the axial fluctuations tend to be dominant, while the outer layers reveal stronger fluctuations along

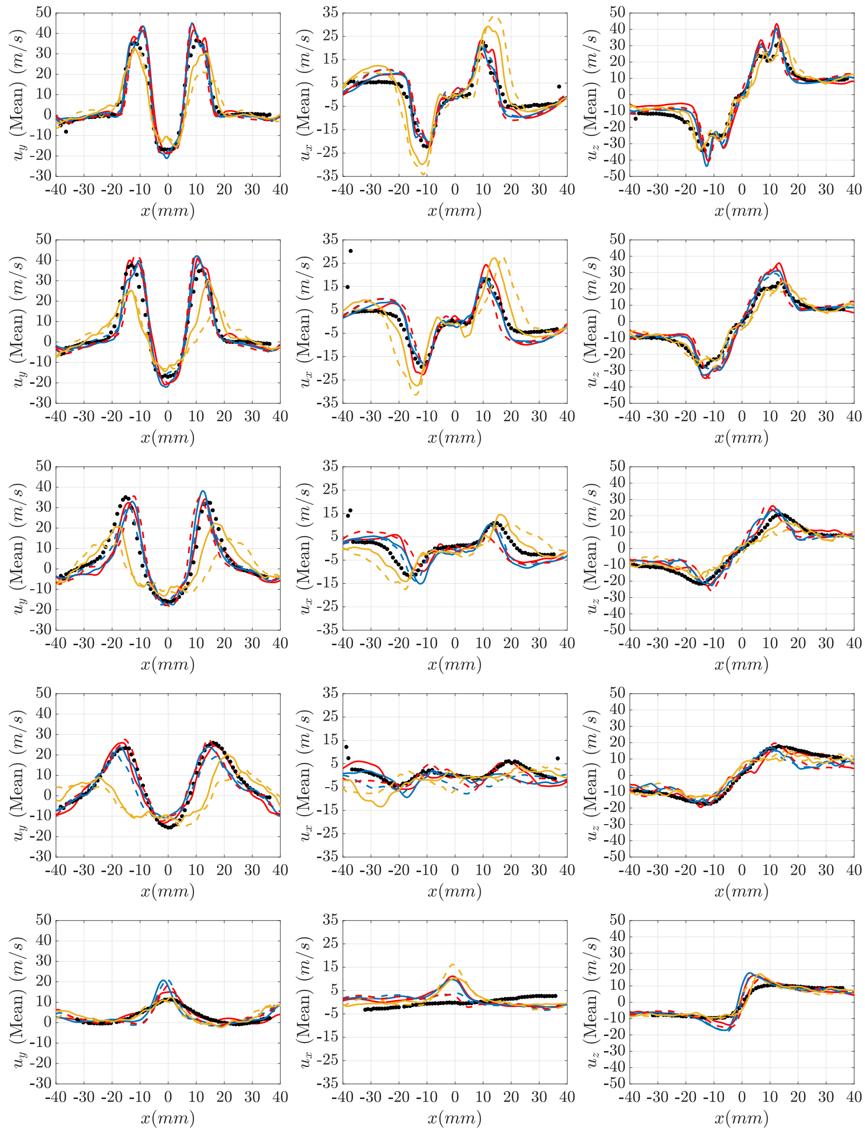

FIG. 8. Time-averaged axial (left), radial (middle) and tangential (right) velocity profiles at $h = 2.5$ mm, $h = 5$ mm, $h = 10$ mm, $h = 20$ mm and $h = 90$ mm from top to bottom rows; —HLLC & Smag.; —AUSM+ & Smag; —KEP & Smag; - - -HLLC & Vreman; - - -AUSM+ & Vreman; - - -KEP & Vreman; ● LDA measurement[44].

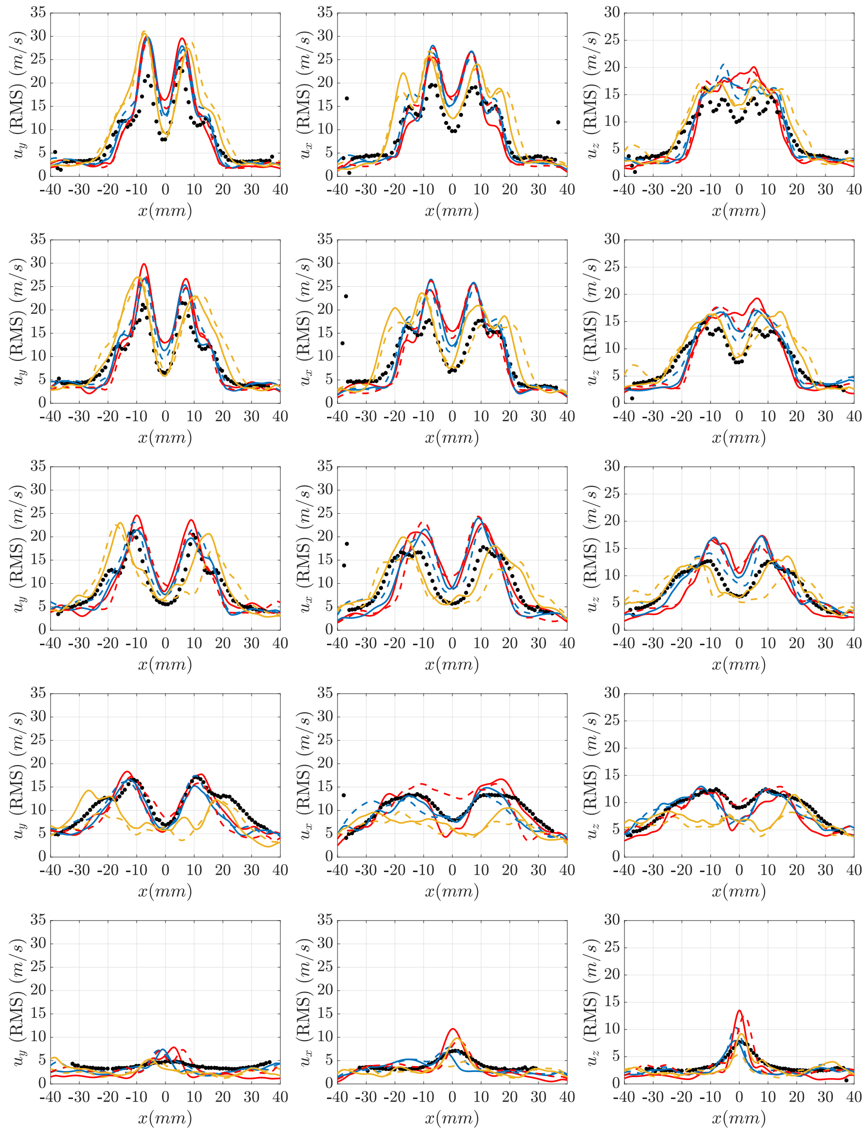

FIG. 9. RMS axial (left), radial (middle) and tangential (right) velocity profiles at $h = 2.5$ mm, $h = 5$ mm, $h = 10$ mm, $h = 20$ mm and $h = 90$ mm from top to bottom rows; —HLLC & Smag.; —AUSM+ & Smag; —KEP & Smag; - - -HLLC & Vreman; - - -AUSM+ & Vreman; - - -KEP & Vreman; • LDA measurement[44].

the radial direction. Additionally, each fluctuation component shows a local minima in the central region where the level of turbulence is much lower. Above the height of $h = 20$ mm, the multiple-peak structure has vanished due to the intense turbulence mixing. We proceed to discuss the error characteristics associated with different numerical and model setups. It is noted that the valleys at the center are not well reproduced in Cases 1-4 and the fluctuation levels inside the IRZ are over-predicted. Previous studies with the consideration of refined LES [49,66] suggested that the over-prediction as such likely results from the insufficiency of small-scale dissipation. Such a prediction deficiency was also recognized in LES of rotating flows[67,68], where the eddy viscosity given by the common SGS model exhibits a similar issue. Park et al.[69] conjectured that this issue may be due to the linear stress-strain relationship of the considered SGS models. In the future, we would like to consider more sophisticated SGS model formulations and examine their feasibilities in the LES of the present flow configuration. Besides the above model issue, the numerical scheme also has a notable impact on the predication accuracy. The cases with the HLLC flux scheme show an excessive damping of fluctuation levels along the outer shear layer at the locations of $h = 10$ and 20 mm. The LES results with the KEP scheme have already contained relatively larger errors in the mean flow and hence these errors are carried forward into the RMS predictions. Despite the error propagation mechanism, the KEP scheme is able to accurately capture the central valleys in the RMS curves. Finally, the LES with the AUSM+ schemes provides better accuracy overall in RMS predictions.

D. Error landscape

The error-landscape methodology was first introduced by Meyers et al.[70] and used more broadly in assessing LES quality[71–73]. The objective is to determine the optimal refinement strategy or the optimal model parameters for a given mesh. The analysis is based on a systematical variation of LES setup parameters (typically SGS model constants and grid resolution) to establish the error behavior as a function of controlling parameters. However, the original error-landscape analysis requires a large number of LES runs, which becomes computationally infeasible for the complex flow configuration considered in this work. Therefore, here we only consider the variants of the numerical scheme and subgrid-scale model as the controlling parameters.

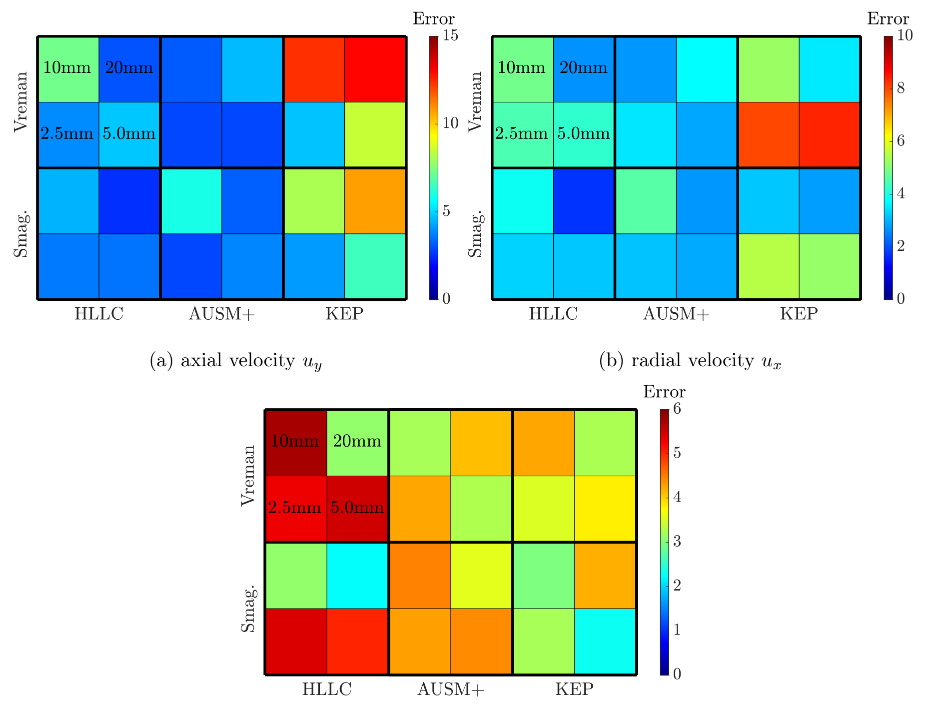

(a) axial velocity u_y

(b) radial velocity u_x

(c) tangential velocity u_z

FIG. 10. Error norms of the time-averaged velocities predicted in LES cases with various setups are presented: (a) axial velocity u_y, (b) radial velocity u_x, and (c) tangential velocity u_z(in each block the values in the sub-block correspond to four measurement heights, respectively).

Figure 10 shows the error norms of time-averaged velocities for different LES setups. The error norm is defined as $(\sum_N |u_{les} - u_{exp}|)/N$, in which N denotes the number of sampling points. Apparently, the error magnitudes depend on both the choice of velocity component and the measurement height for each case. As for the axial and radial velocity components, the error magnitude is smaller with the setups of the HLLC scheme, especially toward the downstream location; however, the HLLC scheme leads to considerable errors for the tangential velocity. In contrast, the KEP scheme provides improved predictions of tangential velocity but results in much larger errors for both the axial and radial velocities. The error given by the AUSM+ scheme is modest but tends to be enlarged at downstream positions. The error maps of RMS velocities for different LES setups are provided in Figure 11. Near the injector exit, all LES setups provide similar error levels for all velocity components. The performance differences among various LES setups become recognizable at downstream locations. The setups of the HLLC scheme no longer hold superior performance. Generally speaking, the AUSM+ scheme has smaller errors in the predictions of RMS velocities. The effect of the SGS model is not obvious, although the Smagorinsky model provides slightly better accuracy for the axial and radial RMS velocities.

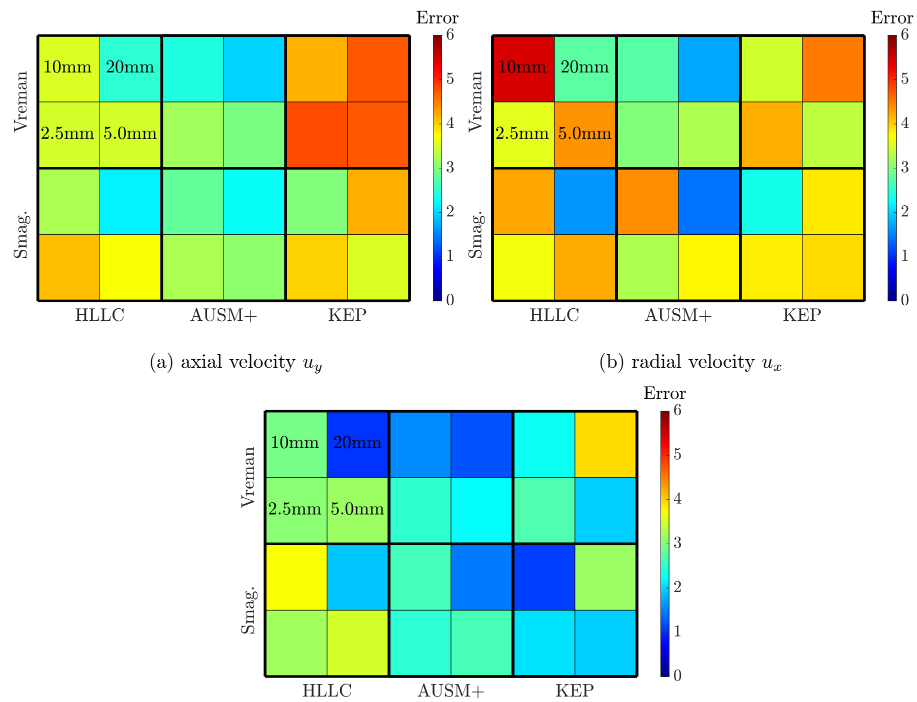

(a) axial velocity u_y

(b) radial velocity u_x

(c) tangential velocity u_z

FIG. 11. Error norms of the RMS predicted in LES cases with various setups are presented: (a) axial velocity u_y, (b) radial velocity u_x, and (c) tangential velocity u_z (in each block the values in the sub-block correspond to four measurement heights, respectively).

V. SUMMARY

The robustness and predictive capability of LES are evaluated in simulations of a complex internal flow configuration in a realistic jet-engine combustor. A number of LES cases are carried out with the consideration of three numerical flux formulations and two commonly used subgrid-scale models. A relatively coarser computational mesh is employed so that the LES results are sensitive to the variants of numerical/model setups and LES errors are thereby manifested. After characterizing and analyzing the LES errors, we obtain several important findings:

- LES is proven to be an effective CFD technique for simulations of complex internal flows (such as the one considered in this study). The predictive capability of LES remains rather robust with a variety of commonly used numerical schemes and subgrid-scale models.
- Compared to the subgrid-scale model, the numerical scheme plays a more prominent role in governing the statistical behaviors of the flow field in LES. It is found in the present study that the properties of the numerical schemes are more relevant to the robustness and accuracy of LES. The effects of the subgrid-scale model are primarily recognized in unsteady flow features, such as vortex breakdown and precessing vortex core.
- For the internal flows considered in this work, blindly pursuing low numerical dissipation could jeopardize the robustness of LES, leading to an inconsistent flow pattern. This is an important lesson learned here, as the finding contradicts the generally accepted notion that a lower dissipative scheme is preferable in LES. It is therefore suggested that caution should be taken when we draw conclusions for the numerical tests that only involve simple flow configurations.
- The anticipated "best" LES setting with the optimal accuracy is not achieved among the considered setups. Error landscape analysis shows that each setup has its strengths and weaknesses, depending on the examined quantity and sampling location. The specific flow configuration favors the Smagorinsky model over the Vreman model, while the dissipative scheme such as HLLC or AUSM+ has superior performance over the kinetic-energy-preserving scheme.

ACKNOWLEDGMENTS

This work is supported by the NSFC Basic Science Center Program for "Multiscale Problems in Nonlinear Mechanics" (No. 11988102). YL acknowledges the startup support from the Chinese Academy of Sciences (CAS) and the financial support from the Bureau of International Cooperation CAS (No. 025GJHZ2022112FN). KW was supported by the National Natural Science Foundation of China (52076008) and the Zhejiang Provincial Natural Science Foundation (LGJ21E060001).

Appendix A: Further assessment of LES quality

To further examine the LES accuracy and robustness, we also evaluate the Pope's criterion[74] for the six LES cases. The metric is defined as the ratio of resolved kinetic energy k to total turbulent kinetic energy $(k + k_{sgs})$. The modeled kinetic energy k_{sgs} can be estimated using the local eddy viscosity μ_t and cell size. The fields of the metric for the different cases are shown in Figure 12. For Cases 1-4, the metric values are above 80% inside the combustor chamber, meaning that the resolution of the flow field there is sufficient. However, it is undesirable to see that the metric values in the swirler region are much lower, therefore indicating RANS-like predictions, especially in the flow passage of the swirler. The profiles of metric values are similar to those obtained in a previous study[45]. The overall quality of LES remains inadequate due to the coarse mesh considered in this study. The inadequacy of resolution is corroborated by the metric values in Cases 5 and 6. Even though the low-dissipation scheme (KEP) is employed, the metric values in fact become smaller. This peculiar finding implies that the smaller turbulent scales liberated by lower dissipation cannot be resolved any more at the present mesh resolution. To examine whether this analysis is plausible, we further evaluated the ratio of subgrid-scale eddy viscosity (μ_{sgs}) to molecular viscosity (μ)[75], and the results are given in Figure 13. As shown, this ratio is indeed much larger in the region of interest in Cases 5 and 6, which confirms the above arguments. In summary, it is learned that *i*) the poor predictions of Cases 5 and 6 are in fact because the smaller scale induced by low dissipation scheme cannot be resolved by the given mesh resolution; and *ii*) the Pope's criterion remains useful for coarse-grid LES to identify the poorer predictions. Caution should be taken when the Pope's criterion is utilized for assessment as it is a genuinely local indicator. Hence, the larger values of the metric in Cases 1-4 can only indicate good local resolution.

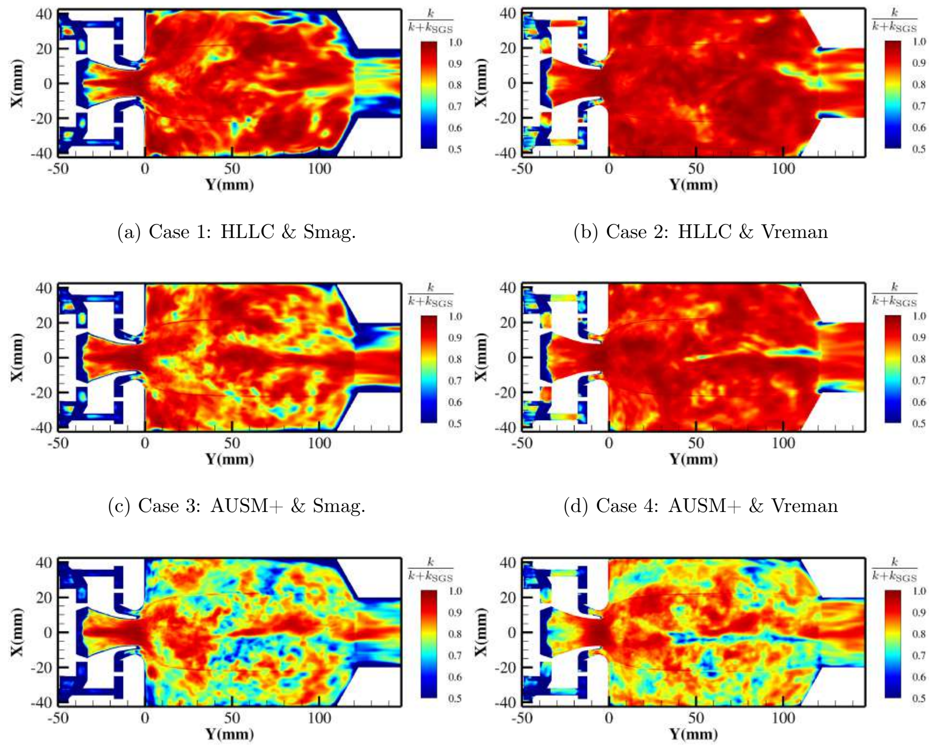

(a) Case 1: HLLC & Smag.

(b) Case 2: HLLC & Vreman

(c) Case 3: AUSM+ & Smag.

(d) Case 4: AUSM+ & Vreman

(e) Case 5: KEP & Smag.

(f) Case 6: KEP & Vreman

FIG. 12. The ratio of resolved kinetic energy (k) to total turbulent kinetic energy ($k + k_{sgs}$), estimated for the six cases: (a) HLLC & Smag., (b) HLLC & Vreman, (c) AUSM+ & Smag., (d) AUSM+ & Vreman, (e) KEP & Smag., and (f) KEP & Vreman.

a. The ratio of subgrid-scale eddy viscosity to molecular viscosity

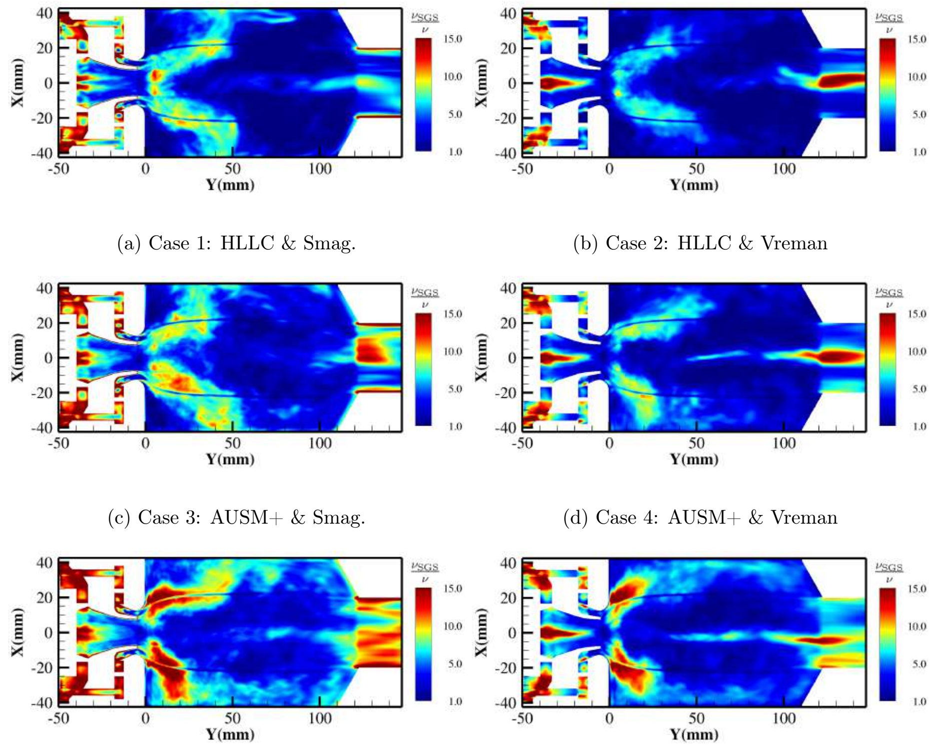

(a) Case 1: HLLC & Smag.

(b) Case 2: HLLC & Vreman

(c) Case 3: AUSM+ & Smag.

(d) Case 4: AUSM+ & Vreman

(e) Case 5: KEP & Smag.

(f) Case 6: KEP & Vreman

FIG. 13. The ratio of subgrid-scale eddy viscosity (μ_{sgs}) to molecular viscosity (μ), evaluated for the six cases: (a) HLLC & Smag., (b) HLLC & Vreman, (c) AUSM+ & Smag., (d) AUSM+ & Vreman, (e) KEP & Smag., and (f) KEP & Vreman.

Appendix B: Near wall mesh resolution

In this appendix, we provide the near-wall resolution for reference. With the wall stress obtained from the employed wall model, the height of the first off-wall grid in the wall unit is evaluated and shown in Fig. 14. As we can see, for most of the wall regions the $y+$ values of the first off-wall grid point are below 10, and therefore the equilibrium wall model reduces to the linear law of the wall in most situations. However, it is worth mentioning that the y^+ estimates only reveal the wall-normal resolution. The resolutions along the other two dimensions are about $y^+ \sim \mathcal{O}(100)$, and hence the LES cases herein remain under-resolved. Although the wall model could play a notable role in the LES, the region of interest in the present study is far from the wall. Moreover, given that the velocity statistics at the chamber inlet have already reached considerable accuracy (see the first rows of Figures 8 and 9), we, therefore, did not place the focus on the wall in this study. The effect of the wall model is left for future investigation.

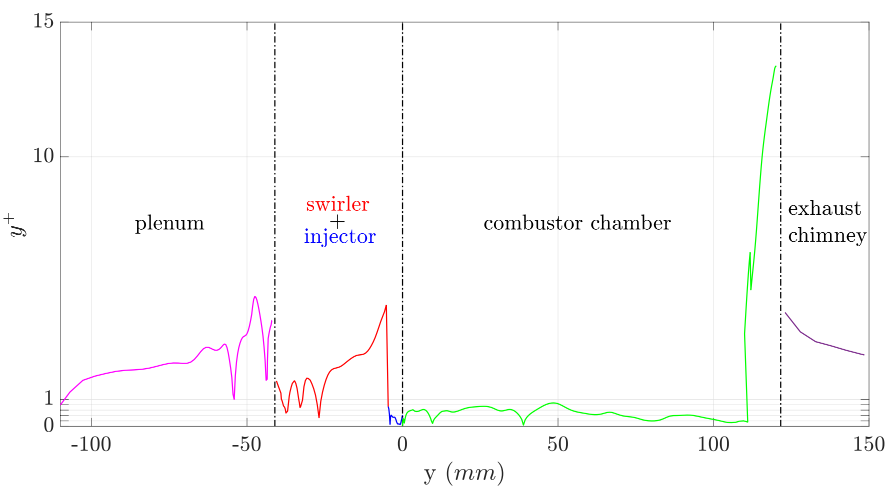

FIG. 14. y^+ the first off-wall grid points as a function of axial location y (the result here is generated with the sidewall data of Case 1; the other cases produce similar results.

REFERENCES

[1]L. Y. Gicquel, G. Staffelbach, and T. Poinsot, "Large eddy simulations of gaseous flames in gas turbine combustion chambers," Progress in Energy and Combustion Science **38**, 782–817 (2012).

[2]A. Mardani, B. Asadi, and A. A. Beige, "Investigation of flame structure and precessing vortex core instability of a gas turbine model combustor with different swirler configurations," Physics of Fluids **34** (2022).

[3]M. Ihme and H. Pitsch, "Modeling of radiation and nitric oxide formation in turbulent nonpremixed flames using a flamelet/progress variable formulation," Physics of Fluids **20**, 055110 (2008).

[4]G. Godel, P. Domingo, and L. Vervisch, "Tabulation of NOx chemistry for large-eddy simulation of non-premixed turbulent flames," Proceedings of the Combustion Institute **32**, 1555–1561 (2009).

[5]C. F. Silva, M. Leyko, F. Nicoud, and S. Moreau, "Assessment of combustion noise in a premixed swirled combustor via large-eddy simulation," Computers & Fluids **78**, 1–9 (2013).

[6]J. Nagao, A. L. Pillai, T. Shoji, S. Tachibana, T. Yokomori, and R. Kurose, "Numerical investigation of wall effects on combustion noise from a lean-premixed hydrogen/air low-swirl flame," Physics of Fluids **35** (2023).

[7]V. Subramanian, P. Domingo, and L. Vervisch, "Large eddy simulation of forced ignition of an annular bluff-body burner," Combustion and Flame **157**, 579–601 (2010).

[8]F. Li, T. Wang, K. Yang, J. Zhang, H. Wang, M. Sun, Z. Wang, and P. Li, "Effect of fuel temperature on mixing characteristics of a kerosene jet injected into a cavity-based supersonic combustor," Physics of Fluids **35** (2023).

[9]L. Esclapez, P. C. Ma, E. Mayhew, R. Xu, S. Stouffer, T. Lee, H. Wang, and M. Ihme, "Fuel effects on lean blow-out in a realistic gas turbine combustor," Combustion and Flame **181**, 82–99 (2017).

[10]A. Panchal and S. Menon, "Large eddy simulation of fuel sensitivity in a realistic spray combustor ii. lean blowout analysis," Combustion and Flame **240**, 112161 (2022).

[11]L. Xing, Y. Li, M. Zheng, T. Gui, Q. Zhang, W. Li, J. Zeng, and H. Xu, "Influence of dual-axial swirler configuration on hydrodynamic stability in combustor," Physics of

Fluids **35** (2023).

[12]T. Poinsot, "Prediction and control of combustion instabilities in real engines," Proceedings of the Combustion Institute **36**, 1–28 (2017).

[13]P. Wolf, G. Staffelbach, L. Y. Gicquel, J.-D. Müller, and T. Poinsot, "Acoustic and large eddy simulation studies of azimuthal modes in annular combustion chambers," Combustion and Flame **159**, 3398–3413 (2012).

[14]Y. Sun, D. Zhao, C. Ji, T. Zhu, Z. Rao, and B. Wang, "Large-eddy simulations of self-excited thermoacoustic instability in a premixed swirling combustor with an outlet nozzle," Physics of Fluids **34** (2022).

[15]S. B. Pope, *Turbulent flows* (Cambridge University Press, 2000).

[16]S. Ghosal, "An analysis of numerical errors in large-eddy simulations of turbulence," Journal of Computational Physics **125**, 187–206 (1996).

[17]B. Vreman, B. Geurts, and H. Kuerten, "Comparision of numerical schemes in large-eddy simulation of the temporal mixing layer," International Journal for Numerical Methods in Fluids **22**, 297–311 (1996).

[18]D. Papadogiannis, F. Duchaine, F. Sicot, L. Gicquel, G. Wang, and S. Moreau, "Large eddy simulation of a high pressure turbine stage: Effects of sub-grid scale modeling and mesh resolution," in *Turbo Expo: Power for Land, Sea, and Air*, Vol. 45615 (American Society of Mechanical Engineers, 2014) p. V02BT39A018.

[19]P. Moin, "Advances in large eddy simulation methodology for complex flows," International Journal of Heat and Fluid Flow **23**, 710–720 (2002).

[20]H. C. Yee, B. Sjögreen, and A. Hadjadj, "Comparative study of three high order schemes for LES of temporally evolving mixing layers," Communications in Computational Physics **12**, 1603–1622 (2012).

[21]E. Johnsen, J. Larsson, A. V. Bhagatwala, W. H. Cabot, P. Moin, B. J. Olson, P. S. Rawat, S. K. Shankar, B. Sjögreen, H. C. Yee, *et al.*, "Assessment of high-resolution methods for numerical simulations of compressible turbulence with shock waves," Journal of Computational Physics **229**, 1213–1237 (2010).

[22]M. El Rafei, L. Könözsy, and Z. Rana, "Investigation of numerical dissipation in classical and implicit large eddy simulations," Aerospace **4**, 59 (2017).

[23]W. Rodi, J. H. Ferziger, M. Breuer, M. Pourquié, *et al.*, "Status of large eddy simulation: results of a workshop," Journal of Fluids Engineering **119**, 248–262 (1997).

[24]S. Iizuka and H. Kondo, "Performance of various sub-grid scale models in large-eddy simulations of turbulent flow over complex terrain," Atmospheric Environment **38**, 7083–7091 (2004).

[25]T. Dairay, E. Lamballais, S. Laizet, and J. C. Vassilicos, "Numerical dissipation vs. subgrid-scale modelling for large eddy simulation," Journal of Computational Physics **337**, 252–274 (2017).

[26]C. B. da Silva and J. C. Pereira, "The effect of subgrid-scale models on the vortices computed from large-eddy simulations," Physics of Fluids **16**, 4506–4534 (2004).

[27]J.-B. Chapelier, B. Wasistho, and C. Scalo, "A coherent vorticity preserving eddy-viscosity correction for large-eddy simulation," Journal of Computational Physics **359**, 164–182 (2018).

[28]D. Foti and K. Duraisamy, "Subgrid-scale characterization and asymptotic behavior of multidimensional upwind schemes for the vorticity transport equations," Physical Review Fluids **6**, 024606 (2021).

[29]H. Kobayashi, "The subgrid-scale models based on coherent structures for rotating homogeneous turbulence and turbulent channel flow," Physics of Fluids **17**, 045104 (2005).

[30]H. Kobayashi, F. Ham, and X. Wu, "Application of a local SGS model based on coherent structures to complex geometries," International Journal of Heat and Fluid Flow **29**, 640–653 (2008).

[31]J. Lu, H. Tang, L. Wang, and F. Peng, "A novel dynamic coherent eddy model and its application to les of a turbulent jet with free surface," Science China Physics, Mechanics and Astronomy **53**, 1671–1680 (2010).

[32]A. Misra and D. I. Pullin, "A vortex-based subgrid stress model for large-eddy simulation," Physics of Fluids **9**, 2443–2454 (1997).

[33]T. Voelkl, D. Pullin, and D. C. Chan, "A physical-space version of the stretched-vortex subgrid-stress model for large-eddy simulation," Physics of Fluids **12**, 1810–1825 (2000).

[34]D. Chung and G. Matheou, "Large-eddy simulation of stratified turbulence. Part I: A vortex-based subgrid-scale model," Journal of the Atmospheric Sciences **71**, 1863–1879 (2014).

[35]Y. Lv, P. C. Ma, and M. Ihme, "On underresolved simulations of compressible turbulence using an entropy-bounded DG method: Solution stabilization, scheme optimization, and benchmark against a finite-volume solver," Computers & Fluids **161**, 89–106 (2018).

[36]T. Barth and P. Frederickson, "Higher order solution of the Euler equations on unstructured grids using quadratic reconstruction," in *28th aerospace sciences meeting* (1990) p. 13.

[37]Y. Lv, "Development of a nonconservative discontinuous Galerkin formulation for simulations of unsteady and turbulent flows," International Journal for Numerical Methods in Fluids **92**, 325–346 (2020).

[38]Y. Lv, X. L. Huang, X. Yang, and X. I. Yang, "Wall-model integrated computational framework for large-eddy simulations of wall-bounded flows," Physics of Fluids **33**, 125120 (2021).

[39]H. Zhang, Y. Chen, and Y. Lv, "Development and validation of a combustion large-eddy-simulation solver based on fully compressible formulation and tabulated chemistry," Aerospace Science and Technology , 107693 (2022).

[40]J. Larsson, S. Kawai, J. Bodart, and I. Bermejo-Moreno, "Large eddy simulation with modeled wall-stress: recent progress and future directions," Mechanical Engineering Reviews **3**, 15–00418 (2016).

[41]X. I. Yang, G. I. Park, and P. Moin, "Log-layer mismatch and modeling of the fluctuating wall stress in wall-modeled large-eddy simulations," Physical review fluids **2**, 104601 (2017).

[42]P. Weigand, W. Meier, X. R. Duan, W. Stricker, and M. Aigner, "Investigations of swirl flames in a gas turbine model combustor: I. Flow field, structures, temperature, and species distributions," Combustion and flame **144**, 205–224 (2006).

[43]W. Meier, X. R. Duan, and P. Weigand, "Investigations of swirl flames in a gas turbine model combustor: II. Turbulence–chemistry interactions," Combustion and Flame **144**, 225–236 (2006).

[44]A. Widenhorn, B. Noll, and M. Aigner, "Numerical study of a non-reacting turbulent flow in a gas-turbine model combustor," in *47th AIAA Aerospace Sciences Meeting including the New Horizons Forum and Aerospace Exposition*, p. 647.

[45]Y. C. See and M. Ihme, "LES investigation of flow field sensitivity in a gas turbine model combustor," in *52nd Aerospace Sciences Meeting* (2014) p. 0621.

[46]P. Wang and X.-S. Bai, "Large eddy simulations of turbulent swirling flows in a dump combustor: a sensitivity study," International Journal for Numerical Methods in Fluids **47**, 99–120 (2005).

[47]G. Lodato, P. Domingo, and L. Vervisch, "Three-dimensional boundary conditions for direct and large-eddy simulation of compressible viscous flows," Journal of Computational Physics **227**, 5105–5143 (2008).

[48]A. Ghani, T. Poinsot, L. Gicquel, and G. Staffelbach, "LES of longitudinal and transverse self-excited combustion instabilities in a bluff-body stabilized turbulent premixed flame," Combustion and Flame **162**, 4075–4083 (2015).

[49]P. Zhang, J.-W. Park, B. Wu, and X. Zhao, "Large eddy simulation/thickened flame model simulations of a lean partially premixed gas turbine model combustor," Combustion Theory and Modelling **25**, 1296–1323 (2021).

[50]E. F. Toro, M. Spruce, and W. Speares, "Restoration of the contact surface in the hll-riemann solver," Shock waves **4**, 25–34 (1994).

[51]M.-S. Liou, "A sequel to AUSM, Part II: AUSM+-up for all speeds," Journal of Computational Physics **214**, 137–170 (2006).

[52]A. Jameson, "Formulation of kinetic energy preserving conservative schemes for gas dynamics and direct numerical simulation of one-dimensional viscous compressible flow in a shock tube using entropy and kinetic energy preserving schemes," Journal of Scientific Computing **34**, 188–208 (2008).

[53]J. Smagorinsky, "General circulation experiments with the primitive equations: I. The basic experiment," Monthly Weather Review **91**, 99–164 (1963).

[54]A. Vreman, "An eddy-viscosity subgrid-scale model for turbulent shear flow: Algebraic theory and applications," Physics of Fluids **16**, 3670–3681 (2004).

[55]G. Lau, G. Yeoh, V. Timchenko, and J. Reizes, "Large-eddy simulation of natural convection in an asymmetrically-heated vertical parallel-plate channel: Assessment of subgrid-scale models," Computers & Fluids **59**, 101–116 (2012).

[56]W. Rozema, H. J. Bae, P. Moin, and R. Verstappen, "Minimum-dissipation models for large-eddy simulation," Physics of Fluids **27**, 085107 (2015).

[57]N. Syred, "A review of oscillation mechanisms and the role of the precessing vortex core (PVC) in swirl combustion systems," Progress in Energy and Combustion Science **32**, 93–161 (2006).

[58]Q. An, W. Y. Kwong, B. D. Geraedts, and A. M. Steinberg, "Coupled dynamics of lift-off and precessing vortex core formation in swirl flames," Combustion and Flame **168**, 228–239 (2016).

[59] M. Vanierschot and G. Ogus, "Experimental investigation of the precessing vortex core in annular swirling jet flows in the transitional regime," Experimental Thermal and Fluid Science **106**, 148–158 (2019).

[60] Y. Huang and V. Yang, "Dynamics and stability of lean-premixed swirl-stabilized combustion," Progress in Energy and Combustion Science **35**, 293–364 (2009).

[61] M. Vanierschot and E. Van den Bulck, "Hysteresis in flow patterns in annular swirling jets," Experimental Thermal and Fluid Science **31**, 513–524 (2007).

[62] J. M. d. Pinho and A. R. Muniz, "The effect of subgrid-scale modeling on les of turbulent coaxial jets," Journal of the Brazilian Society of Mechanical Sciences and Engineering **43**, 1–12 (2021).

[63] M. Escudier and J. Keller, "Recirculation in swirling flow-a manifestation of vortex breakdown," AIAA Journal **23**, 111–116 (1985).

[64] G. Bulat, W. Jones, and S. Navarro-Martinez, "Large eddy simulations of isothermal confined swirling flow in an industrial gas-turbine," International Journal of Heat and Fluid Flow **51**, 50–64 (2015).

[65] A. Benim, S. Iqbal, A. Nahavandi, W. Meier, A. Wiedermann, and F. Joos, "Analysis of turbulent swirling flow in an isothermal gas turbine combustor model," in *Turbo Expo: Power for Land, Sea, and Air*, Vol. 45684 (American Society of Mechanical Engineers, 2014) p. V04AT04A001.

[66] Y. C. See, *Analysis of Hydrodynamic Instabilities and Combustion Dynamics in Turbulent Reacting Flows*, Ph.D. thesis (2014).

[67] A. C. Benim, M. Escudier, A. Nahavandi, A. Nickson, K. J. Syed, and F. Joos, "Experimental and numerical investigation of isothermal flow in an idealized swirl combustor," International Journal of Numerical Methods for Heat & Fluid Flow (2010).

[68] H. Xianbei, L. Zhuqing, Y. Wei, L. Yaojun, and Y. Zixuan, "A cubic nonlinear subgrid-scale model for large eddy simulation," Journal of Fluids Engineering **139** (2017).

[69] N. Park, S. Lee, J. Lee, and H. Choi, "A dynamic subgrid-scale eddy viscosity model with a global model coefficient," Physics of Fluids **18**, 125109 (2006).

[70] J. Meyers, B. J. Geurts, and M. Baelmans, "Database analysis of errors in large-eddy simulation," Physics of Fluids **15**, 2740–2755 (2003).

[71] M. Klein, J. Meyers, and B. J. Geurts, "Assessment of LES quality measures using the error landscape approach," Quality and Reliability of Large-Eddy Simulations , 131–142

(2008).

[72]J. Meyers, "Error-landscape assessment of large-eddy simulations: a review of the methodology," Journal of Scientific Computing **49**, 65–77 (2011).

[73]A. Kempf, B. J. Geurts, and J. Oefelein, "Error analysis of large-eddy simulation of the turbulent non-premixed sydney bluff-body flame," Combustion and Flame **158**, 2408–2419 (2011).

[74]S. B. Pope, "Ten questions concerning the large-eddy simulation of turbulent flows," New Journal of Physics **6**, 35 (2004).

[75]I. Celik, M. Klein, and J. Janicka, "Assessment measures for engineering LES applications," Journal of Fluids Engineering **131**, 031102 (2009).